Multiple metabolic pathways fuel the truncated tricarboxylic acid cycle of the prostate to sustain constant citrate production and secretion

Lilianne Frégeau-Proulx [1,2,3], Aurélie Lacouture [1,2,3], Line Berthiaume [1,3], Cindy Weidmann [1,3], Mario Harvey [1,3], Kevin Gonthier [1,2,3], Jean-François Pelletier [3,4], Bertrand Neveu [3,4], Cynthia Jobin [1,2,3], Dominic Bastien [3,4], Alain Bergeron [3,4,5], Yves Fradet [3,4,5], Louis Lacombe [3,4,5], Isabelle Laverdière [3,4,6,7], Chantal Atallah [8], Frédéric Pouliot [3,4,5], Étienne Audet-Walsh [1,2,3],*

ABSTRACT

Objective: The prostate is metabolically unique: it produces high levels of citrate for secretion via a truncated tricarboxylic acid (TCA) cycle to maintain male fertility. In prostate cancer (PCa), this phenotype is reprogrammed, making it an interesting therapeutic target. However, how the truncated prostate TCA cycle works is still not completely understood.

Methods: We optimized targeted metabolomics in mouse and human organoid models in *ex vivo* primary culture. We then used stable isotope tracer analyses to identify the pathways that fuel citrate synthesis.

Results: First, mouse and human organoids were shown to recapitulate the unique citrate-secretory program of the prostate, thus representing a novel model that reproduces this unusual metabolic profile. Using stable isotope tracer analysis, several key nutrients were shown to allow the completion of the prostate TCA cycle, revealing a much more complex metabolic profile than originally anticipated. Indeed, along with the known pathway of aspartate replenishing oxaloacetate, glutamine was shown to fuel citrate synthesis through both glutaminolysis and reductive carboxylation in a GLS1-dependent manner. In human organoids, aspartate entered the TCA cycle at the malate entry point, upstream of oxaloacetate. Our results demonstrate that the citrate-secretory phenotype of prostate organoids is supported by the known aspartate—oxaloacetate—citrate pathway, but also by at least three additional pathways: glutaminolysis, reductive carboxylation, and aspartate—malate conversion.

Conclusions: Our results add a significant new dimension to the prostate citrate-secretory phenotype, with at least four distinct pathways being involved in citrate synthesis. Better understanding this distinctive citrate metabolic program will have applications in both male fertility as well as in the development of novel targeted anti-metabolic therapies for PCa.

1. INTRODUCTION

Glucose, amino acids, and fatty acids can fuel mitochondrial activity through the tricarboxylic acid (TCA) cycle for ATP production. This cycle begins with the transfer of the two-carbon acetyl group from acetyl-CoA to the four-carbon acceptor oxaloacetate, which replenishes the two carbons lost during one cycle. This reaction forms the six-carbon citrate molecule, and the cycle continues. The prostate gland is metabolically unique: luminal epithelial cells have a truncated TCA cycle to produce, accumulate, and secrete high levels of citrate (Figure 1A) [1,2]. It has been proposed that these cells accumulate high zinc levels that inhibit the mitochondrial aconitase enzyme (ACO2),

thus impairing citrate usage in the TCA cycle to allow its secretion [1—4]. This specialized citrate-secretory phenotype is an important function of the prostate gland for human reproduction because it maintains semen pH, buffers calcium ions, and participates in the coagulation/de-coagulation process. For example, in semen plasma, citrate has a high affinity for ions such as calcium, magnesium, and zinc. It acts as a buffer for calcium ions, and it is the major regulator of ionized calcium concentration in the semen [5]. Because calcium concentration is important to sperm count and motility, changes in citrate secretion has important implications for male fertility [6]. Seminal citrate levels are thus positively correlated with sperm count, morphology, motility, and volume [7].

[1]Endocrinology — Nephrology Research Axis, CHU de Québec — Université Laval Research Center, Québec, QC, Canada [2]Department of Molecular Medicine, Faculty of Medicine, Université Laval, Québec, QC, Canada [3]Centre de Recherche sur le Cancer de l'Université Laval, Québec, QC, Canada [4]Oncology Research Axis, CHU de Québec — Université Laval Research Center, Québec, QC, Canada [5]Department of Surgery, Faculty of Medicine, Université Laval, Québec, QC, Canada [6]Faculty of Pharmacy, Université Laval, Québec, QC, Canada [7]Department of Pharmacy, CHU de Québec — Université Laval, Québec, QC, Canada [8]Department of Pathology, CHU de Québec — Université Laval, Québec, QC, Canada

*Corresponding author. Centre de Recherche du CHU de Québec — Université Laval, 2705 Boulevard Laurier, Room R-4714, Québec, QC, G1V 4G2, Canada. E-mail: etienne.audet-walsh@crchudequebec.ulaval.ca (É. Audet-Walsh).

Original Article

In addition to its role in male fertility, the alteration of the citrate-secretory phenotype is also tightly linked to prostate cancer (PCa). Indeed, during malignant transformation, citrate metabolism is reprogrammed, leading to a 10- to 100-fold decrease in citrate levels in tumors compared to peri-tumor tissues [3,8—10]. This loss of the citrate-secretory phenotype occurs in virtually all PCa cases, highlighting it as a hallmark of PCa [1—4,8—15]. Accordingly, decreases in prostate citrate levels can be detected using magnetic resonance spectroscopy, and several studies have identified this decrease in citrate as a biomarker for PCa diagnosis [16—18]. Moreover, lower intratumor citrate concentrations have been associated with shorter recurrence-free survival, suggesting that reprogramming of citrate is not only linked to carcinogenesis but also to PCa progression [19,20]. It is currently thought that cancer cells restore a functional TCA cycle to sustain their aberrant energy requirement for proliferation [21]. Understanding citrate metabolism, how it is regulated, and how it can be reprogrammed, is thus important for both human fertility and cancer research.

However, it is still unclear how this metabolic profile works in the normal prostate. Notably, if citrate is secreted, the two carbons from acetyl-coA and the four carbons from oxaloacetate are lost from the cycle. In that context, at least two sources of carbon are needed to replenish the carbon pool required for continuous citrate secretion. Glucose and fatty acids can be used to replenish acetyl-coA. In cellular contexts other than the prostate, several amino acids were shown to fuel the TCA cycle at downstream entry points, such as glutamate, generated from glutamine, which allows synthesis of α-ketoglutarate (αKG). However, the current model of prostate metabolism is based on aspartate being the only nutrient replenishing the four missing carbons from the cycle by allowing oxaloacetate replenishment, thus assuming a heavily truncated cycle, a mostly inactive electron transport chain, and low/absent mitochondrial respiration [1,2,22]. Another intriguing question arising from this model is how these cells produce their ATP if mitochondrial respiration is non-functional. Initial reports using rat prostate lysates mostly described non-functional mitochondria and suggested that prostate epithelial cells mainly depend on aerobic glycolysis (lactate production) for energy synthesis [23,24].

Several recent observations highlight the necessity to readdress how prostate metabolism works. First, state-of-the-art mitochondrial respiration assays have demonstrated that human prostate tissues exhibit mitochondrial respiration despite exhibiting a truncated TCA cycle [25,26]. These respiratory assays suggested a bypass of the first steps of the TCA cycle, catalyzed by ACO2 and mitochondrial isocitrate dehydrogenases (IDH2 and IDH3). This is consistent with a blockade of the cycle right after citrate synthesis. However, these mitochondrial assays suggested a functional TCA cycle after αKG synthesis, indicating that some nutrients could provide fuel early in the cycle to allow a specific cycle to operate rather than only replenishing oxaloacetate. Second, the idea that prostate epithelial cells exhibit low or absent respiration and rely on high aerobic glycolysis is hard to reconcile with recent *in vivo* imaging data from fluorine-18 fluorodeoxyglucose, a readout of glycolytic activity, which shows low activity in the normal prostate or low-grade cancers [27—29]. Altogether, these results suggest that prostate epithelial cells exhibit specialized mitochondria designed to support citrate production and secretion, but that they also exhibit a non-canonical TCA cycle that sustains "partial" respiration. To our knowledge, the current model is mostly based on murine tissue lysates [23,24,30—33]; the nutrients that provide carbons in the TCA cycle in live prostate epithelial cells, including human models, have not yet been studied.

To better understand the truncated TCA cycle of the prostate, we leveraged mouse and human prostate organoid models combined with mass spectrometry (MS)-based metabolomics. First, we show that these organoids recapitulate the unique citrate-secretory program of this gland, being—to our knowledge—a unique model that reproduces this unusual metabolic profile. Using stable isotope tracer analysis, we identified several key nutrients that allow completion of the truncated TCA cycle in these prostate organoids and revealed a much more complex metabolic profile than originally anticipated. These results, obtained with both mouse and human prostate organoids, support the model depicting that the unique TCA cycle of the prostate is much more flexible than anticipated, with several nutrients fueling it at different entry points to support both citrate production and energy synthesis.

2. MATERIAL AND METHODS

2.1. Purification of mouse prostate epithelial cells for primary culture

All mouse work was performed according to Université Laval's Animal Research and Ethics Committee's guidelines and regulations. Mice (C57BL/6) were bred, housed in a 12 h light:12 h dark cycle at 22 °C, and handled at the animal care facility of the Centre de recherche du CHU de Québec — Université Laval. Purification of prostate epithelial cells was adapted from the protocol of Lacouture et al. for purification of mammary epithelial cells [34]. All volumes shown below are for purification of epithelial cells using four mice at 12 weeks of age. After sacrifice, prostates were surgically collected and maintained in 1× complete HBSS solution (HBSS + 2% FBS + 10 mM HEPES + 100 U/mL penicillin and 100 µg/mL streptomycin [Wisent]). Prostates were then minced with scissors under a biological hood and transferred to a tube containing 4 mL of a 1× complete EpiCult-B mouse medium with 5% FBS (EpiCult basal medium [STEMCELL technologies], 10 ng/mL Recombinant human EGF [STEMCELL technologies], 10 ng/mL recombinant human bFGF [STEMCELL technologies], 4 µg/mL heparin [Sigma—Aldrich], 100 U/mL penicillin, 100 µg/mL streptomycin, 10% EpiCult proliferation supplement [STEMCELL technologies]) with 1 mL of 1× Gentle Collagenase/Hyaluronidase solution (STEMCELL technologies) for a 2 h incubation at 37 °C. The solution was then gently mixed by pipetting followed by a centrifugation at 350 *g* for 5 min. The supernatant was discarded and the pellet resuspended with 1 mL of warm 0.25% trypsin—EDTA (Wisent). After 1 min of gentle pipetting, 4 mL of 0.25% trypsin—EDTA was added followed by 1 min of gentle pipetting. After 1 h of incubation on ice, 10 mL of 1× complete HBSS solution was added; the tube was inverted two or three times before centrifugation at 350 *g* for 5 min. After removal of the supernatant, 2 mL of warm dispase (5 U/mL — STEMCELL technologies) and 200 µL of 1 mg/mL of DNase I (Roche) were added. After pipetting for 1—3 min to dissociate clumps, 10 mL of cold 1× complete HBSS solution was added and the tube inverted 2—3 times before filtration through a 40 µm Cell Strainer (Falcon). The cells were centrifugated for 5 min at 350 *g* and were resuspended in 1 mL of 1× complete EpiCult-B mouse medium with 5% FBS for counting. Cells were purified using the EasySep Mouse PE Positive Selection kit II (#17666, STEMCELL technologies) according to the manufacturer's protocol with 10 µL of CD49-PE antibody (#555736, BD Biosciences) for 20×10^6 cells. The obtained cells were centrifuged and counted.

2.2. Primary culture of mouse epithelial cells

For two-dimensional culture, the purified cells were centrifuged 5 min at 350 *g* and resuspended in Keratinocyte serum-free medium (KSFM), with

1× penicillin and streptomycin [GIBCO], 10 μM of the anti-ROCK inhibitor Y-27632 (Tocris), cholera toxin (4 ng/mL) (Sigma—Aldrich), and the TGF-β pathway inhibitor A 83-01 (500 nM) (MilliporeSigma). The suspension was plated in 0.003% poly-L-lysine-coated (Sigma—Aldrich) culture dishes and kept in a 37 °C incubator with 5% CO_2. The medium was changed every three days. When reaching confluence, cells were detached with TrypLE (GIBCO) supplemented with 10 μM Y-27632 for 5 min at 37 °C and scraped gently before plating in poly-L-lysine coated culture dishes. For three-dimensional culture, cells were resuspended in complete EpiCult-B mouse medium with 5% FBS and used to produce 40 μL droplets containing 75% of growth factor reduced Matrigel (Corning). Each droplet, containing 30,000 to 60,000 cells depending on the experiment, was seeded using cold tips in a warm culture dish. After plates were incubated 15 min upside down at 37 °C, warm complete EpiCult-B mouse medium with 5% FBS was added to each well to cover Matrigel droplets. After 24 h, the medium was changed for serum-free EpiCult-B mouse medium (EpiCult basal medium, 10% EpiCult proliferation supplement, 10 ng/mL recombinant human EGF, 10 ng/mL recombinant human bFGF, 4 μg/mL heparin, 100 U/mL penicillin, and 100 μg/mL streptomycin) and replaced every three days.

2.3. Cell labeling and flow cytometry analysis

Before and after mouse epithelial cell purification, 250,000 cells were resuspended in 100 μL of FACS buffer (5% FBS + 0.05% sodium azide in PBS) and stained with CD24-APC (clone M1/69, BioLegend) and CD49f-PE (clone GoH3, Biosciences), or the isotype control antibodies, at the manufacturer's recommended dilution. Antibodies were incubated at room temperature for 30 min and then cells were washed twice in FACS buffer. Data were acquired using a BD FACSCelesta™ Flow Cytometer and BD FACSDiva™ software version 8.0.1.1 (Becton, Dickinson and Company). Data analysis was performed using FlowJo™ version 10.7.1 (Becton, Dickinson and Company). Ten thousand events were acquired for each sample. Isotype controls were used to set the gates.

2.4. Histology, immunofluorescence, and microscopy analyses

Matrigel droplets were fixed in 3% agarose. Briefly, 1 mL of 1× PBS was added in each well and droplets were scraped gently and moved to a 1.5 mL micro-centrifuge tube. Matrigel droplets were centrifuged at 2500 g for 2 min at 4 °C. The supernatant was discarded, and the pellet was washed with 1.5 mL of 1× PBS, and centrifuged at 2500 g for 2 min at 4 °C. Matrigel droplets were fixed with 4% paraformaldehyde for 1 h at room temperature and then centrifuged at 2500 g for 3 min at 4 °C. The supernatant was discarded and a few drops of 3% agarose were added. The fixed agarose drops were transferred to histological cassettes and were again fixed overnight in 10% formalin before being embedded in paraffin (Laboratoire de pathologie de l'Hôtel-Dieu de Québec). The paraffin-embedded organoids were cut into 5 μm sections with a microtome (HistoCore MULTICUT 14051856372, Leica) for H&E staining. Images were taken with an EVOS™ M5000 Imaging System (ThermoFisher Scientific).

For immunofluorescence, each slide was deparaffinized and rehydrated. An antigen retrieval step was performed with the Diva Decloaker (DV2005 L2J) by Biocare and the slides were incubated overnight at 60 °C. A blocking step was also performed with TBS 1× — 1% BSA — 5% FBS for 2 h at room temperature. The primary antibodies for CK5 (1:250, sc-32721, Santa Cruz Biotechnology) and CK8/18 (1:1000, MA5-32118, Invitrogen) were incubated overnight in TBS 1× — 1% BSA — 2.5% FBS at 4 °C. After washing, secondary antibodies goat anti-rabbit IgG Alexa Fluor 555 (1:2000, A-21428, Invitrogen) and goat anti-mouse IgG Alexa Fluor 488 (1:2000, A-

11001, Invitrogen) were incubated for 1 h at room temperature. Finally, FluoromounT-G with DAPI (00-4959-52, ThermoFisher Scientific) was added. Images were taken with an EVOS™ M5000 Imaging System (ThermoFisher Scientific).

2.5. Cell viability assay

AlamarBlue Cell Viability Reagent (#1100, Invitrogen) was used to determine cell viability with and without trypsin dissociation. Organoids without dissociation were scraped in complete Epicult media, and 10% AlamarBlue Cell Viability Reagent was added to each well before incubation at 37 °C for 30 min. For dissociation, trypsin was added to the organoids for 3 min before harvest in media. Organoids were then incubated at 37 °C for 30 min with 10% AlamarBlue Cell Viability Reagent. Wells with media, Matrigel, and AlamarBlue but without organoids were used as negative controls. Finally, fluorescence was measured at 570 nm of excitation and 585 nm of emission using a spectrophotometer. Student's t-tests were used to evaluate statistical significance.

2.6. Human primary prostate cell culture conditions

Human prostate tissues were obtained, with consent, from men undergoing radical prostatectomy as treatment for their cancer. This research was approved by the research ethics committee of the CHU de Québec — Université Laval (Project 2021-5661). Briefly, after resection, 14G-punch biopsies (1—4) were taken in the prostate under the supervision of a pathologist and put into 1× complete HBSS. Biopsies were transferred to the lab and then processed as described for enzymatic digestion of mouse prostates. Cells were suspended in KSFM with 10 μM of the anti-ROCK inhibitor Y-27632, cholera toxin (4 ng/mL), and the TGF-b pathway inhibitor A 83-01 (500 nM). Thereafter, they were seeded at cell densities ranging between 250,000 and 500,000 in poly-L-lysine-treated 10 cm culture dishes; medium was changed twice a week. For passages, cells were detached with TrypLE supplemented with 10 μM Y-27632. For three-dimensional culture, cells were passaged using TrypLE and resuspended after centrifugation in complete human organoid medium (complete KSFM, 1× penicillin and streptomycin, 4% B27 supplements [STEMCELL technologies], 10 μM Calcitriol [Cayman Chemical], 10 nM testosterone, and 10 μM Y-27632) and used to produce 40 μL droplets containing 75% of growth-factor—reduced Matrigel. Each droplet, containing 15,000 to 30,000 cells depending on the experiment, was seeded using cold pipette tips in a warm culture dish. After plates were incubated for 15 min upside down at 37 °C, warm complete human organoid media was added to each well to cover the Matrigel droplets. Media was renewed twice a week for the duration of the experiments.

2.7. Gas chromatography — mass spectrometry

Mouse and human prostate organoids were cultured for two weeks with and without incubation with ^{13}C-labeled nutrients (during the last 72 h) and then harvested for GC—MS analyses. When harvested without dissociation, 1 mL of media was first harvested, centrifuged 5 min at 10,000 g, and the supernatant was transferred to a new 1.5 mL tube. In parallel, organoids were rinsed with ice-cold saline on ice before being harvested on dry ice with dry-ice-cold 80% MeOH. Extracellular media and organoids were both flash frozen and stored at −80 °C until GC—MS analysis. When harvested with dissociation, media was harvested in a 15 mL tube and trypsin was added to the organoids. Organoid plates were returned to 37 °C for 3 min. Dissociation was finalized by returning media culture to the respective organoid well, pipetting it up and down 10 times, and transferring it to a new 15 mL tube. Organoids with media were centrifuged 5 min at

Original Article

800 *g*. The supernatant, containing organoid secretion, was then transferred to a new tube, flash frozen, and stored at −80 °C. Organoids were washed once with ice-cold saline, centrifuged 5 min at 800 *g* at 4 °C, and then mixed with dry-ice-cold 80% MeOH. All samples were kept at −80 °C until analyses.

On the day of analyses, organoids were lysed by sonication and centrifuged at 20,000 *g* for 10 min [34]. For culture media, 200 μL of media was mixed with 400 μL of dry-ice-cold 80% MeOH before centrifugation at 20,000 *g* for 10 min. After centrifugation of either media or organoids, supernatant was transferred into a new tube containing the internal standard Myristic acid-d27 (CDN Isotopes, Canada), to which 700 μL acetonitrile (ACN) was added. Samples were vortexed, centrifuged, and the supernatant was recovered to be dried using nitrogen gas. A two-step derivatization protocol was then performed: 1) methoxyamination with the method described by Fiehn [35] and 2) silylation with MTBSTFA/TBDMCS using the modified method from Patel et al. [36]. Finally, samples were analyzed with GC–MS using an Agilent 8890 GC equipped with a DB5-MS + DG capillary column connected to an Agilent 5977B MS operating under electron impact (EI) ionization at 70 eV (Agilent Technologies, Santa Clara, CA, USA). For all samples, 1 μL was injected in split mode at 250 °C. Helium was the carrier gas (flow rate of 1 mL/min). The temperature of the GC oven was held at 50 °C for 2 min, then raised to 150 °C at a rate of 20 °C/min for 5 min, and from 150 °C to 300 °C at a rate of 10 °C/min; column temperature was then kept constant at 300 °C for another 10 min. The MS source and quadrupole were held at 230 °C and 150 °C, respectively, and the detector was operated in scanning mode for mass range 50–600 Da at a signal rate of 5.1 scans/sec. Analyses were made using the Agilent MassHunter Workstation Software. After deconvolution, metabolites were identified using the NIST/EPA/NIH Mass Spectral Library (NIST 2017, Gaithersburg, MD, USA). To perform absolute quantification, TCA cycle intermediate standards were used in parallel; other metabolites were shown in relative quantification after normalization with the internal standard (myristic acid-d27).

For ^{13}C-glucose (#CLM-1396-PK, Cambridge Isotope Laboratories, Inc.), ^{13}C-aspartate (#48999, Sigma–Aldrich), and ^{13}C-glutamine (#CLM-1822-H-0.1MG, Cambridge Isotope Laboratories, Inc.), we used concentrations of 10 mM, 1 mM, and 2 mM in culture media, respectively. They were injected directly into either KSFM or EpiCult-B mouse media, both containing unlabeled glucose and glutamine but low levels of aspartate (not detectable by GC–MS). After incubation with tracers, organoids were harvested and analyzed by GC–MS as described above. For treatment with inhibitors, ^{13}C-nutrients were added simultaneously to 6 μM of bis-2-(5-phenylacetamido-1,3,4-thiadiazol-2-yl)ethyl sulfide (BPTES; Selleckchem). Note that in parallel with being harvested for GC–MS analyses, additional organoids were dissociated for cell counting that was used to normalize metabolomic data for cellular content.

For metabolomic analyses of mouse tissues, adult mice were sacrificed and organs harvested before being flash frozen and stored at −80 °C. Tissues were ground with a mortar using liquid nitrogen on dry ice. Tissue powder was weighed and resuspended in dry-ice-cold 80% MeOH before being processed as described above for organoids. Student's *t*-tests were used to evaluate statistical significance.

3. RESULTS AND DISCUSSION

3.1. Describing the metabolic profile of the mouse prostate
We first studied the metabolic profile of the mouse prostate, focusing on the TCA cycle, and compared it to several other tissues, including liver, heart, and brown adipose tissue. Citrate was highly enriched in the prostate, with an average of 2.2 μmol/g (Figure 1B). These levels were 28- to 52-fold higher than those in all the other tissues studied, which had levels near ∼0.05 μmol/g (50 ηmol/g). We next measured the levels of the TCA cycle intermediate cis-aconitate. While its levels were lower compared to citrate in the prostate, with an average of 0.23 μmol/g (Figure 1C), it was four to 10 times higher than any other tissue. These results suggest that citrate strongly accumulates in the prostate, but that a significant proportion can nevertheless continue in the TCA cycle. Succinate, fumarate, and malate levels were similar across all the tissues tested, including the prostate (Figure 1D–F). Other TCA cycle intermediates were either not detected or could not be interrogated using our GC–MS approach in mouse tissues. If the cycle was completely truncated in the prostate, as expected from the actual model, one would assume that downstream intermediates would be much lower in terms of absolute concentrations. These results suggest that nutrients downstream of citrate but upstream of oxaloacetate allow the completion of the TCA cycle in the prostate.

Another intriguing question is whether prostate epithelial cells exhibit mitochondrial respiration and, if not, how do they produce ATP. Based on rat prostate extracts, it is thought that these cells mainly depend on aerobic glycolysis for energy synthesis [23,24]. However, *in vivo* imaging data shows low glycolytic activity in the normal prostate [27–29]. Furthermore, recent work has demonstrated that prostate tissues have detectable mitochondrial respiration despite exhibiting a truncated TCA cycle [26]. We hypothesized that the dependency on aerobic glycolysis would not be as strong as currently assumed, and thus we also measured lactate (Figure 1G). The prostate, along with the testis, showed the lowest lactate levels (Figure 1G). Such a result does not indicate that this organ relies principally on aerobic glycolysis for energy synthesis. Other metabolites were measured, including several amino acids, but none showed specific enrichment in the prostate (Supplemental Figure S1). Altogether, these results suggest that despite massive citrate production, the prostate nevertheless exhibits significant levels of the different TCA cycle intermediates, suggesting an alternative cycle that is not solely composed of oxaloacetate and citrate.

3.2. Mouse prostate organoids exhibit the citrate-secretory phenotype
To better understand the prostate-specific citrate metabolic program, we next optimized a protocol for FACS-free purification of mouse prostate epithelial cells and their primary culture *ex vivo* (see section two for details). In brief, the prostate is harvested and processed through sequential enzymatic digestions to obtain a single-cell suspension. Epithelial cells are then purified using magnetic beads. This protocol allows high enrichment of basal and luminal epithelial cells, as shown by flow cytometry (Figure 2A and Supplemental Figure S2A). After purification, cells can be plated for primary culture in two dimensions (Supplemental Figure S2B) or be used for organoid culture in three dimensions (Figure 2B). Organoids began to be visible after three days in culture and continuously grew for 12–14 days, at which time they reached their maximum size (Figure 2B). The prostate gland is known to require androgens to activate the androgen receptor (AR), which promotes growth and survival, and testosterone had a significant impact on organoid growth (Figure 2B and C). This positive regulation by AR was associated with an increased size of the organoids, but with no change in the total number of organoids (Supplemental Figure S2C). Histological staining with hematoxylin and eosin (H&E) shows the glandular structure of the prostate organoids, *i.e.,* the organization of cells surrounding an internal lumen, which are
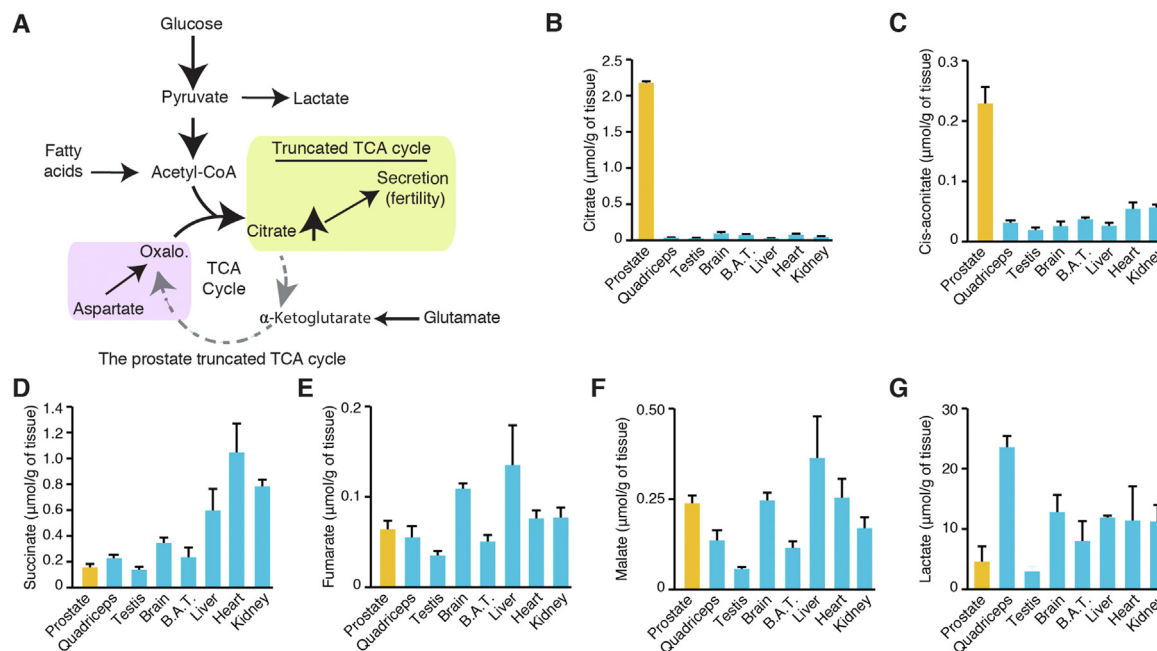
Figure 1: The prostate exhibits a unique truncated TCA cycle that supports massive citrate production. A) Current working model of the prostate's truncated TCA cycle. Citrate is massively produced by prostate epithelial cells and secreted into the seminal fluid; this is a well-known phenotype associated with fertility. Several nutrients could fuel the prostate TCA cycle, including glucose, fatty acids, glutamate, and aspartate. It is currently assumed that glucose and aspartate are the major carbon sources required for citrate production and secretion. (B–G) Targeted metabolomics of TCA cycle intermediates and lactate in various mouse tissues. Results are shown as the average ± SEM of two independent experiments comprising organs from seven mice. Results are shown for the prostate (yellow) and other organs (blue) in μmol/g of tissues. BAT: Brown adipose tissue. Additional metabolites quantified are available in Supplemental Figure S1.

further increased with the androgen testosterone (Figure 2C). Given the positive impact of androgens on organoid growth, all subsequent experiments were performed in the presence of testosterone.

The prostate gland secretes within internal lumens, and the presence of such a structure in prostate organoids led us to hypothesize that these organoids could recapitulate the *in vivo* secretory functions of the prostate and thus secrete citrate in these lumens. To test this hypothesis, we performed gas chromatography — mass spectrometry (GC–MS) targeted metabolomics in organoids to detect citrate secretion within their lumen. With an intact organoid, the internal lumen is not connected to the extracellular media. However, we hypothesized that dissociation of the 3D architecture with trypsin would allow internal secretions to be released to capture metabolites secreted from luminal cells (Figure 2D). In the absence of dissociation, several metabolites were quantified in the extracellular media, including low levels of citrate as well as other TCA cycle intermediates, *i.e.*, αKG and malate (Figure 2E and Supplemental Figure S2D). After organoid dissociation, the levels of several metabolites did not change while others had significantly increased (Figure 2E and Supplemental Figure S2D). Of all the metabolites tested, citrate had the biggest change (3.25 fold) compared to all other differences, which were all below a 1.73-fold change, except for malate (2.42 fold). It must also be kept in mind that the volume of luminal secretion is believed to be low compared to the volume of extracellular media. Thus, to allow changes in the extracellular concentrations, a metabolite must be present at high concentrations within luminal secretion. These results show that prostate organoids secrete citrate as well as other metabolites into their internal lumen. To avoid the possibility that dissociation—even if brief—would induce cell death and the release of metabolites, we studied cellular viability following our dissociation protocol. No

differences were observed with or without the dissociation procedures (Supplemental Figure S2E). Overall, these results show a unique prostate model that exhibits the distinctive citrate-secretory phenotype of the prostate *ex vivo*.

3.3. Glucose, glutamine, and aspartate can fuel citrate production in mouse prostate organoids

Next, we wanted to determine the different nutrients providing carbon to the prostate-specific TCA cycle. To do so, we used stable isotope tracer analysis using ^{13}C-labeled nutrients. We focused on glucose and aspartate, which are currently thought to be the major carbon sources required for citrate secretion [11,33] (Figure 3A). We also studied glutamine, the most abundant amino acid in circulation, which could also sustain mitochondrial respiration by replenishing αKG (Figure 3A). Organoids were thus incubated with $^{13}C_6$-glucose, $^{13}C_{1-4}$-aspartate, or $^{13}C_5$-glutamine for 72 h, a time-point that maximizes labeling compared to shorter periods (data not shown). Glucose (10 mM) and glutamine (2 mM) concentrations were close to the physiological concentrations in circulation, while aspartate (1 mM) was close to the intra-prostatic tissue concentration (Figure S1). After incubation with the different tracers, organoids were dissociated to harvest both organoids and their luminal secretion. Note that upon GC–MS analysis, aspartate was shown to be labeled with either one, two, three, or four ^{13}C, but usually with only one or two ^{13}C (Supplemental Figure S3A).

In organoids, the use of $^{13}C_6$-glucose and $^{13}C_5$-glutamine led to a 24% and 20% labeling in citrate, respectively, while labeling with aspartate was minor (<1%) (Figure 3B). As expected, citrate was mainly labeled in m + 2 and m + 4 from $^{13}C_6$-glucose and $^{13}C_5$-glutamine, respectively, thus fueling a "canonical" TCA cycle. $^{13}C_5$-glutamine also
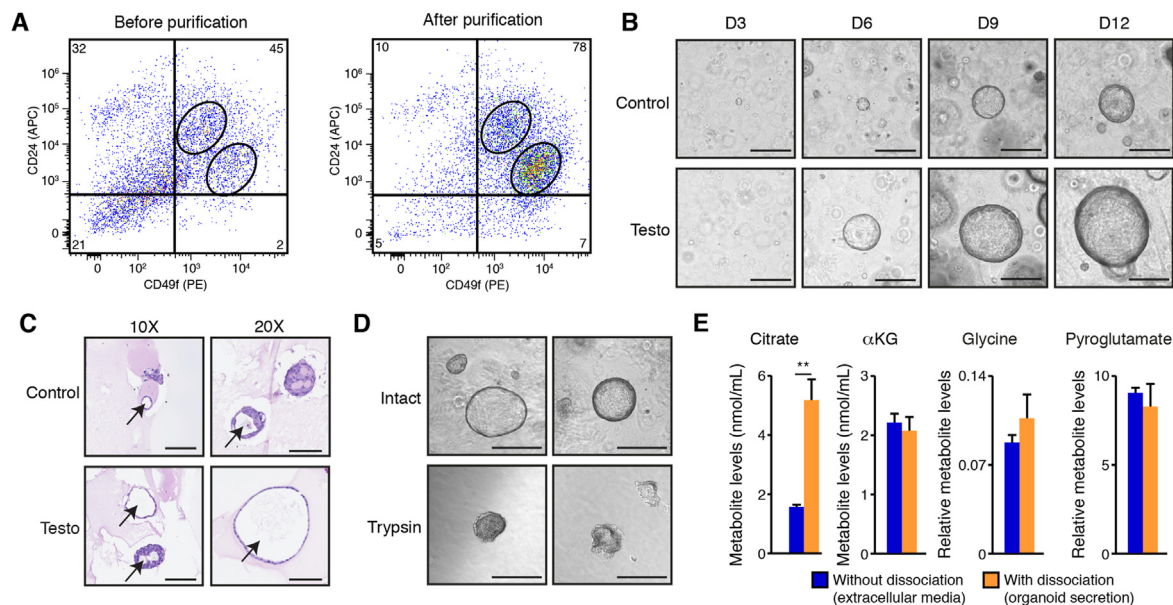
Figure 2: Primary mouse prostate organoids exhibit the citrate-secretory phenotype. A) Flow cytometry analyses of basal epithelial cells (CD49f^high/CD24^intermediate) and luminal epithelial cells (CD49f^intermediate/CD24^high) before and after purification. Numbers in the corners are percentages. One representative experiment of two independent experiments is shown. B) Brightfield visualization of organoids over 12 days in three-dimensional culture with and without testosterone, an androgen treatment. Testosterone induces a significant increase in organoid size without changing the number of organoids (quantification of organoid numbers and sizes is available in Supplemental Figure S2C). Testo: Testosterone treatment. Scale bars = 300 μm. C) H&E visualization of mouse prostate organoids after 14 days in culture, with and without testosterone. Arrows show the presence of internal lumen in these organoids. Scale bars = 125 μm and 100 μm, respectively, for 10× and 20× view. Note that during the fixation process, bigger organoids tend to lose their circular architecture. D) Brief treatment with trypsin (3 min) disrupts the three-dimensional architecture of mouse prostate organoids to allow connection of the internal lumen with the extracellular media. Scale bars = 300 μm. E) GC—MS metabolite quantification in extracellular culture media of mouse prostate organoids treated with testosterone, with and without dissociation, as shown in D. With dissociation, this media contains luminal secretion. Results are shown as the average ± SEM of one representative experiment performed in quadruplicates, out of five independent experiments. **$p < 0.01$.

showed enrichment in citrate m + 5, possibly indicating that reductive carboxylation can occur to support citrate production (Figure 3B). Cis-aconitate, αKG, and fumarate were below limits of quantification in organoids, but succinate and malate were quantifiable. As we expected given the truncation of the cycle, a much lower labeling in succinate and malate by $^{13}C_6$-glucose was detected, mostly labeling them in m + 2. (Figure 3C and 3D). $^{13}C_5$-glutamine mostly led to succinate and malate labeling in m + 4, consistent with its entry point from αKG (Figure 3A). Altogether, these results demonstrate that glutamine along with glucose is a major nutrient fueling TCA cycle activity in prostate organoids, bypassing the ACO2 inhibited step of the cycle and allowing a functional cycle to operate. This is important, as glutamine-supported TCA cycle activity allows mitochondrial respiration and ATP synthesis [37,38]. This probably explains why prostate mitochondria have detectable respiration [25,26] and also why prostate epithelial cells do not solely rely on aerobic glycolysis.

Labeling from $^{13}C_6$-glucose downstream citrate was detected, indicating that a small fraction of the carbons used from glucose to produce citrate can also be used downstream in the TCA cycle, consistent with in vivo results showing cis-aconitate in the prostate (Figure 1).

In parallel, metabolomics was also performed in luminal secretion, notably in secreted citrate. $^{13}C_6$-glucose and $^{13}C_5$-glutamine showed labeling patterns similar to those seen in organoids, with ∼20—25% labeling in secreted citrate isotopomers (Figure 3E). In addition, $^{13}C_{1-4}$-aspartate led to significant labeling of secreted citrate, with ∼12% labeled citrate (Figure 3E). These results confirm that aspartate can contribute to the production of citrate for secretion, though to a lesser extent compared to glucose and glutamine. The fraction of ^{13}C labeling

in succinate and malate remained the same in secreted metabolites (Supplemental Figs. S3B and S3C) compared to intra-organoid levels (Figure 3C and 3D).

To better understand the relationship between glutamine and citrate synthesis, we next performed metabolomics using mouse prostate organoids treated or not with BPTES. This drug inhibits the glutaminase 1 enzyme (GLS1), which allows the conversion of glutamine into glutamate that can then be converted to αKG to enter the TCA cycle. After 11 days in culture, organoids were treated for 72 h with 6 μM, which did not induce major changes in organoid growth or viability (Supplemental Figure S3D). Interestingly, treatment with BPTES significantly decreased carbon flux from glutamine into glutamate, the product of GLS1, and blocked flux into the TCA cycle, confirming that GLS1 is an essential entry point of glutamine metabolism in prostate organoids for citrate synthesis (Figure 3F).

Altogether, these results using organoids suggest that the prostate citrate-secretory profile is more complex than originally anticipated. First, mouse prostate organoids exhibit a TCA cycle than is not only comprised of oxaloacetate-citrate. Second, glutamine is a major nutrient fueling the truncated TCA cycle at the αKG entry point—a well-known pathway that allows mitochondrial respiration. Third, glutamine could also fuel citrate production through reductive carboxylation. Fourth, as initially reported, both glucose and aspartate indeed support citrate production and secretion. Fifth, contrary to what was assumed, despite supporting citrate secretion, aspartate is not essential for citrate synthesis. Indeed, media used for organoid culture contains only low aspartate levels (in the low μM range). Results from Figures 2 and 3 thus indicate that aspartate is not, per se, an essential
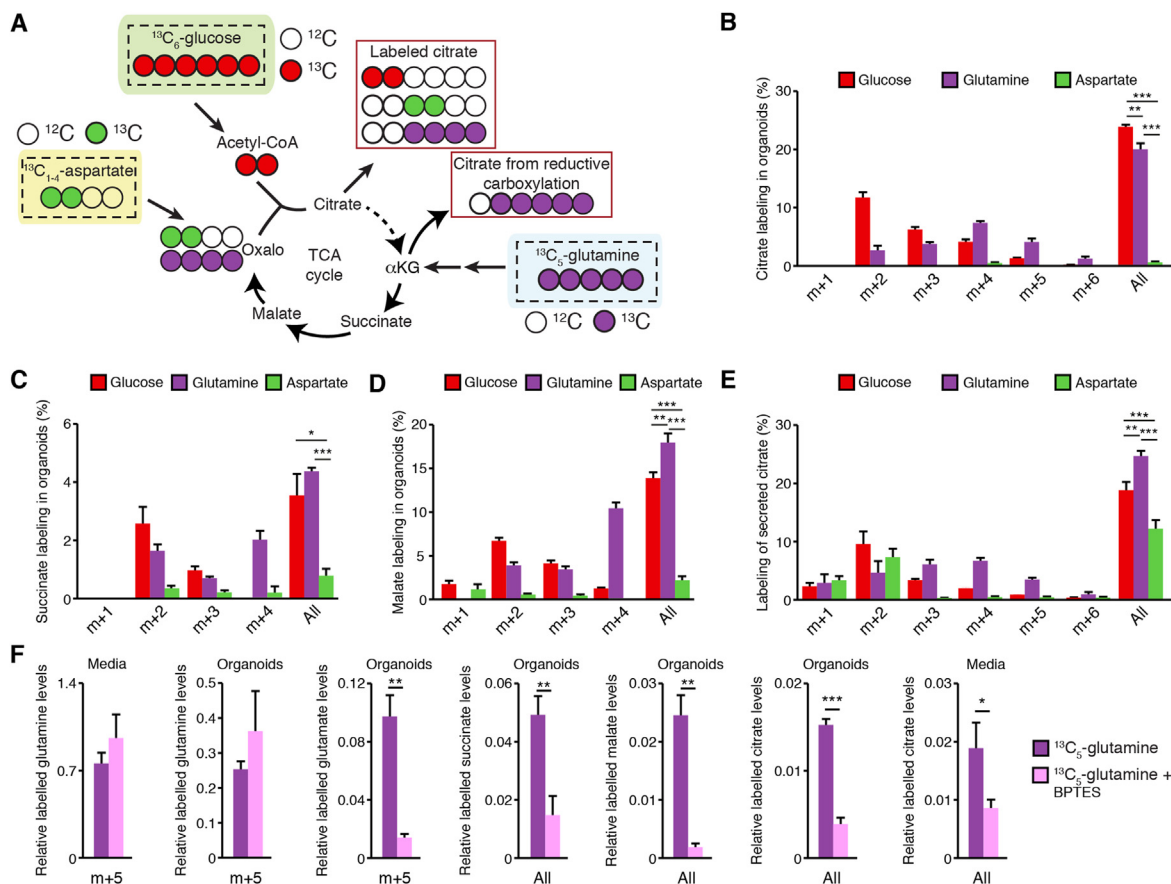
Figure 3: Contribution of glucose, glutamine, and aspartate to the prostate organoid TCA cycle. A) Schematic representation of respective carbon contributions when organoids are supplemented with $^{13}C_6$-glucose, $^{13}C_5$-glutamine, or $^{13}C_{1-4}$-aspartate, assuming aspartate carbons enter the cycle via oxaloacetate. For graphical purposes, aspartate is shown as $^{13}C_2$-aspartate, but labeling in B−E can be observed from $^{13}C_1$-, $^{13}C_2$-, $^{13}C_3$-, or $^{13}C_4$-aspartate. Stable isotope tracer analyses in organoids using in parallel these three tracers are then shown for citrate (B), succinate (C), and malate (D), as well for extracellular levels of citrate (E). After 11 days in culture, organoids were incubated for 72 h with $^{13}C_6$-glucose, $^{13}C_5$-glutamine, or $^{13}C_{1-4}$-aspartate before being dissociated and harvested for GC−MS analyses. "All" indicates the sum of all shown isotopomers for a given metabolite. Statistics were only calculated using the sum of all isotopomers of a given metabolite. Results are shown as the average $\pm$ SEM of one representative experiment performed in triplicate out of three independent experiments. For these tracer experiments, note that organoids were cultured in parallel with the different ^{13}C-labeled nutrients. Secreted succinate and malate labeling is shown in Supplemental Figure S3. F) Stable isotope tracer analysis in organoids following 72 h exposure to $^{13}C_5$-glutamine, with and without the GLS1 inhibitor BPTES. After 72 h, organoids and luminal secretion (media) were harvested for metabolomics. For glutamine and glutamate, m + 5 labeling is shown; for TCA cycle intermediates, as labeling patterns were more complex (as shown in B−E), the sum of total labeling is shown (as shown in B−E). Results are shown as the average $\pm$ SEM of one representative experiment performed in triplicates out of two independent experiments. $***p < 0.001$; $**p < 0.01$; $*p < 0.05$.

amino acid required for massive citrate production and secretion. However, when supplemented, aspartate did support citrate production for secretion. Consequently, the distinctive citrate-secretory phenotype of mouse prostate organoids is not only comprised of one metabolic pathway, but it can be supported by at least three alternative pathways, including glutaminolysis, reductive carboxylation, and aspartate—oxaloacetate conversion. How these results obtained in mouse models apply to the human prostate is currently unknown.

3.4. Stable isotope tracer analyses in human prostate organoids
Finally, we wanted to determine whether the results obtained with mouse prostate organoids also hold for human prostate organoids. Indeed, the citrate-secretory phenotype of the prostate is well conserved in mammals, but the molecular mechanisms allowing citrate production and secretion could be different. To accomplish this, fresh human prostate biopsies in patients with PCa were obtained from two surgically resected prostates. Biopsies were taken after surgery in zones without any evidence of PCa and as distant as possible from

zones with cancer cells. Biopsies were enzymatically digested to obtain a single-cell suspension before being used for primary culture in two dimensions. The enrichment of epithelial cells was performed using culture media that favors these cells rather than stromal cells (Supplemental Figure S4A), as described by others [39,40]. After three passages, cells were plated to be grown as organoids. As seen with mouse prostate organoids, human prostate organoids began to be visible after three days in culture, reached their maximum size after two weeks in culture (Figure 4A), and formed glandular structures with the presence of internal lumen (Figure 4B). As characterized by others [41,42], despite being generally smaller compared to mouse prostate organoids, human prostate organoids were composed principally of basal and luminal (secretory) epithelial cells, as shown by CK5 and CK8/18 labeling, respectively (Supplemental Figure S4B).

Next, GC−MS analyses were performed with and without organoid dissociation to free internal luminal secretions (Figure 4C and Supplemental Figure S4C). Interestingly, citrate levels decreased in organoids following dissociation, while it increased in the media after
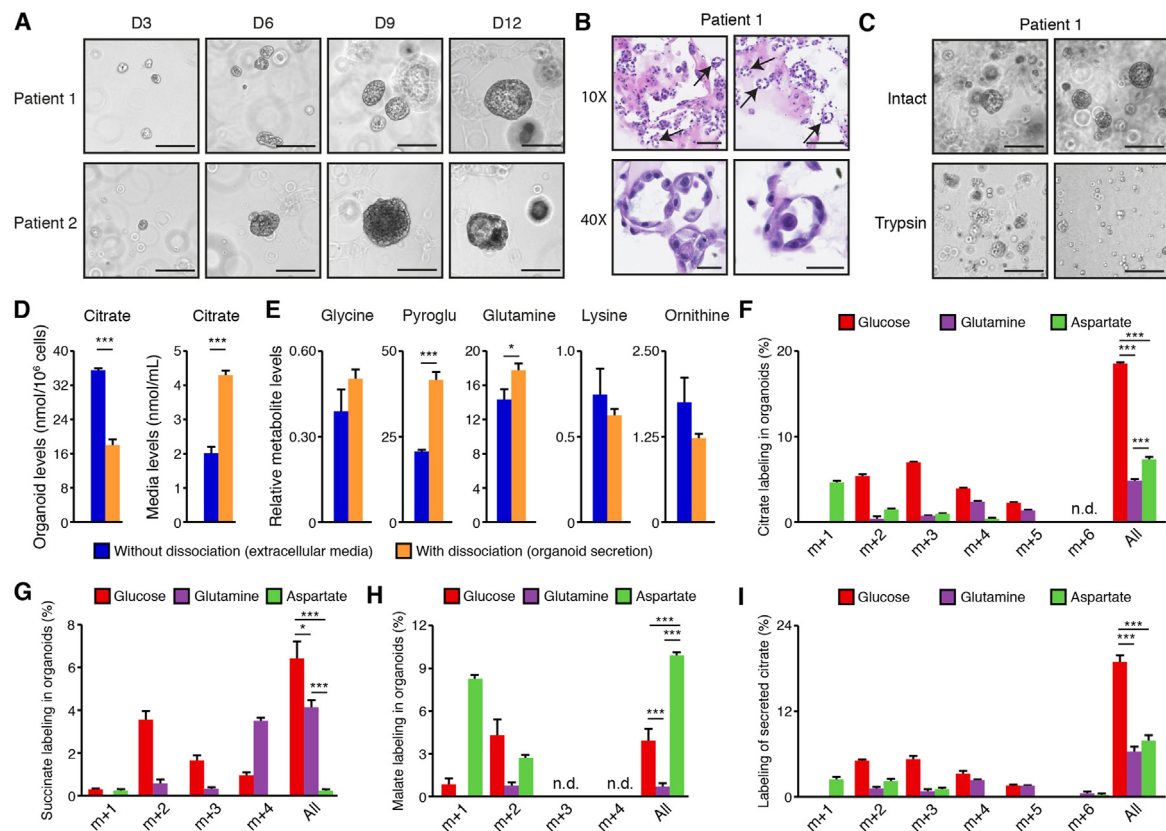
Figure 4: Metabolomics analyses in human prostate organoids. A) Brightfield visualization of normal human prostate organoids over 12 days in three-dimensional culture. Organoid cultures derived from two different human patients are shown. Scale bars = 200 μm. B) H&E visualization of patient-derived prostate organoids showing the presence of internal lumen, demonstrated by black arrows. Scale bars = 125 μm and 50 μm, respectively, for 10× and 40× view. C) Brief treatment with trypsin (3 min) disrupts the three-dimensional architecture of human prostate organoids to allow connection of the internal lumen with the extracellular media. Scale bars = 200 μm. Representative images from patient #1 are shown and images for patient-derived organoids from patient #2 are available in Supplemental Figure S4C. D) Intra-organoid and extracellular citrate level quantification by GC—MS, with and without dissociation as shown in C. With dissociation, media contains luminal secretion. E) GC—MS metabolite quantification in extracellular culture media of human prostate organoids, with and without dissociation, as shown in C. For D and E, results are shown as the average ± SEM of one representative experiment performed in triplicate out of three independent experiments. Pyroglu: pyroglutamate. Stable isotope tracer analysis in organoids using $^{13}C_6$-glucose, $^{13}C_5$-glutamine, or $^{13}C_{1-4}$-aspartate tracers is then shown for intra-organoid citrate (F), succinate (G), and malate (H) levels, as well as for secreted citrate levels (I). For results shown in F—I, organoids were dissociated before GC—MS metabolomics quantifications. Results are shown as the average ± SEM of one representative experiment performed in triplicates out of two independent experiments for patient #1. For these tracer experiments, note that organoids were cultured in parallel with the different ^{13}C-labeled nutrients. Similar results were obtained with organoids from patient #2 and are shown in Supplemental Figure S4. N.d.: not detectable or below the limit of quantification. "All" indicates the sum of all shown isotopomers for a given metabolite. Statistics were only calculated using the sum of all isotopomers of a given metabolite. ***$p < 0.001$; **$p < 0.01$; *$p < 0.05$.

dissociation, reinforcing the idea that citrate is released from internal lumens after dissociation (Figure 4D). Several other metabolites were detected in the extracellular media, some being increased and some being unchanged by dissociation (Figure 4E and Supplemental Figure S4D). Finally, stable isotope tracer analyses were performed with a 72 h treatment with $^{13}C_6$-glucose, $^{13}C_{1-4}$-aspartate, or $^{13}C_5$-glutamine before dissociation and harvest of luminal secretion and organoids. In human organoids, citrate labeling was predominantly from $^{13}C_6$-glucose; there was up to 18% labeling (Figure 4F). $^{13}C_{1-4}$-aspartate and $^{13}C_5$-glutamine both led to 5—8% labeling in intracellular organoid citrate levels (Figure 4F). Intracellular levels of succinate and malate were also detectable (Figure 4G and 4H). For succinate, carbon labeling was similar to what was observed in mouse organoids (Figure 3C), indicating a major contribution of both glucose and glutamine to their carbon pools and as anticipated from the different entry points of these nutrients in the TCA cycle (Figure 3A).

For malate, labeling patterns were different in human organoids compared to mouse organoids. First, only modest labeling with $^{13}C_5$-glutamine was observed. Second, $^{13}C_{1-4}$-aspartate labeling patterns indicated that aspartate is a major contributor to malate synthesis in human organoids, with up to 14% labeling. We cannot rule out that these differences between mouse and human organoids are not caused by differences in culture conditions. Most notably, due to the limited availability of fresh tissue, human prostate epithelial cells are first expanded in 2D culture before being passaged for organoid formation. In that context, it is possible that some changes occur compared to the native prostate gland *in vivo*. Nevertheless, these results suggest that, in human prostate organoids, aspartate fuels the TCA cycle upstream of oxaloacetate to synthesize malate and supports citrate secretion in a system that looks like the malate—aspartate shuttle. This shuttle, composed of four enzymes and two transporters, allows the shuttling of electrons between the cytosol and the
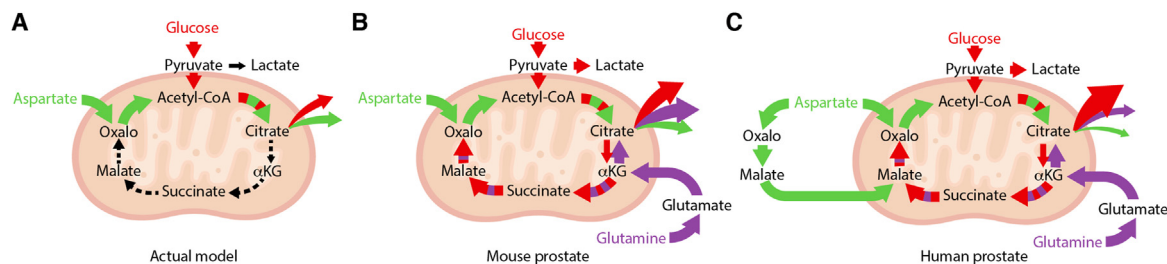
Figure 5: Updated working model of citrate metabolism in mouse and human prostate. A) The current working model of prostate metabolism describes a truncated TCA cycle that allows massive citrate secretion into the semen. In this model, glucose and aspartate are both essential for acetyl-CoA and oxaloacetate synthesis to sustain citrate synthesis by citrate synthase. However, metabolomics using mouse prostate tissues and mouse and human prostate organoids showed herein dress a more complex profile in the mouse (B) and human (C) prostate. First, aspartate is not essential for citrate synthesis. Second, citrate, but also downstream intermediates, can be produced using glucose, aspartate, and glutamine as carbon sources. Glutamine was revealed to be a significant nutrient contributing to citrate secretion by both allowing α-ketoglutarate (αKG) production for synthesis of downstream intermediates and by reductive carboxylation of αKG. The current study also revealed that aspartate can enter at different entry points of the TCA cycle. In human prostate organoids, aspartate appears to enter the TCA cycle in a way that mimics the malate—aspartate shuttle, providing malate for the synthesis of citrate. Sizes of the arrows indicate the respective contribution of the different nutrients to the TCA cycle and to citrate secretion.

mitochondria in the form of reduced malate, to replenish mitochondrial pools of NADH. Cytosolic GOT1 uses aspartate to synthesize oxaloacetate that can be reduced to malate by MDH1. This cytosolic malate is then shuttled to the mitochondria to be oxidized back to oxaloacetate by MDH2, and it can then be used for citrate synthesis in the prostate. Furthermore, ^{13}C-labeling in secreted citrate was very similar to intracellular human organoid labeling, with major labeling with $^{13}C_6$-glucose and similar contributions from both $^{13}C_5$-glutamine and $^{13}C_{1-4}$-aspartate (Figure 4I). Labeling patterns of secreted succinate and malate in human organoids were similar to intracellular labeling (Supplemental Figure 4E). Finally, labeling patterns of glutamine, aspartate, and glucose were validated using a second patient-derived organoid model (Supplemental Figure 4F). Results show high homogeneity between patient-derived organoids, again indicative of major contribution of all three nutrients to the truncated TCA cycle and an entry point for aspartate through malate in these prostate models.

4. CONCLUSION

In summary, using stable isotope tracer analyses in mouse and human prostate models, we demonstrated that they retain a prostate citrate-secretory profile, and that this profile is far more complex than originally anticipated for the prostate gland. First, our results support the model where aspartate can replenish intermediates from the TCA cycle, notably citrate, but suggest that the prostate TCA cycle is not solely dependent on aspartate to replenish the four carbons of oxaloacetate to continuously produce citrate. Interestingly, aspartate also fueled the TCA cycle at the malate entry point. Next, glutamine was shown to be a major nutrient used to synthesize citrate from both oxidative and reductive pathways. Importantly, glutamine usage to replenish carbons at the αKG entry point allows mitochondrial respiration, probably explaining at least in part how prostate epithelial cells can regenerate their ATP. Overall, our results add a significant new dimension to the prostate citrate-secretory phenotype that can be supported by the known aspartate—oxaloacetate—citrate pathway, but also by three additional pathways: glutaminolysis, reductive carboxylation, and aspartate—malate conversion. We thus present updated working models of mouse and human prostate citrate metabolism (Figure 5). Future work will be important to validate these findings *in vivo*.

Future studies will allow a better understanding of prostate metabolism in both human physiology and disease. Indeed, better comprehension of the prostate's distinctive citrate metabolic program will have

potential applications in both male fertility and clinical management of PCa. Imaging analysis of intra-prostatic citrate levels showed that decreased levels of this metabolite are associated with PCa progression [19,20]. However, citrate is often studied individually or with other metabolites such as choline in imaging studies, but restored citrate flux through the TCA cycle is predicted to increase downstream TCA intermediates, such as malate and fumarate. It would be interesting to see whether the ratio of citrate with TCA metabolites specifically can better predict PCa prognosis. Moreover, better understanding how the unique citrate metabolic profile of the prostate is reprogrammed in PCa might also allow the development of novel targeted anti-metabolic therapies for PCa.

AUTHOR CONTRIBUTIONS

L.F.P. performed experiments, analyzed results, and helped write the manuscript. A.L., L.B., and C.W. performed experiments, developed methods, analyzed results, helped to write the manuscript, and provided intellectual input. K.G., M.H., J.-F.P., and B.N. performed experiments and provided intellectual input. C.J. and D.B. helped to perform experiments. A.B., Y.F., L.L., and F.P. performed the surgeries and provided intellectual input. I.L. provided equipment for experiments and intellectual input. C.A. produced pathology reports and provided intellectual input. F.P. helped conceive the project and provided intellectual input. E.A.W conceived the project, analyzed data, secured funding, and wrote the manuscript. All authors contributed to the manuscript and approved it for submission.

ACKNOWLEDGMENTS

Original Article

CONFLICT OF INTEREST

The authors declare that the research was conducted in the absence of any commercial or financial relationships that could be construed as a potential conflict of interest.

APPENDIX A. SUPPLEMENTARY DATA

Supplementary data to this article can be found online at https://doi.org/10.1016/j.molmet.2022.101516.

REFERENCES

[1] Costello, L.C., Franklin, R.B., Jan 2017. Decreased zinc in the development and progression of malignancy: an important common relationship and potential for prevention and treatment of carcinomas. Expert Opinion on Therapeutic Targets 21(1):51–66. https://doi.org/10.1080/14728222.2017.1265506.

[2] Cutruzzola, F., Giardina, G., Marani, M., Macone, A., Paiardini, A., Rinaldo, S., et al., 2017. Glucose metabolism in the progression of prostate cancer. Frontiers in Physiology 8:97. https://doi.org/10.3389/fphys.2017.00097.

[3] Costello, L.C., Franklin, R.B., Feng, P., Jun 2005. Mitochondrial function, zinc, and intermediary metabolism relationships in normal prostate and prostate cancer. Mitochondrion 5(3):143–153. https://doi.org/10.1016/j.mito.2005.02.001.

[4] Massie, C.E., Mills, I.G., Lynch, A.G., Feb 2017. The importance of DNA methylation in prostate cancer development. The Journal of Steroid Biochemistry and Molecular Biology 166:1–15. https://doi.org/10.1016/j.jsbmb.2016.04.009.

[5] Owen, D.H., Katz, D.F., Jul-Aug 2005. A review of the physical and chemical properties of human semen and the formulation of a semen simulant. Journal of Andrology 26(4):459–469. https://doi.org/10.2164/jandrol.04104.

[6] Beigi Harchegani, A., Irandoost, A., Mirnamniha, M., Rahmani, H., Tahmasbpour, E., Shahriary, A., Jan 2019. Possible mechanisms for the effects of calcium deficiency on male infertility. International Journal of Fertility and Sterility 12(4):267–272. https://doi.org/10.22074/ijfs.2019.5420.

[7] Shemshaki, G., Murthy, A.S.N., Malini, S.S., Apr-Jun 2021. Assessment and establishment of correlation between reactive oxidation species, citric acid, and fructose level in infertile male individuals: a machine-learning approach. Journal of Human Reproductive Sciences 14(2):129–136. https://doi.org/10.4103/jhrs.jhrs_26_21.

[8] Twum-Ampofo, J., Fu, D.X., Passaniti, A., Hussain, A., Siddiqui, M.M., Feb 22 2016. Metabolic targets for potential prostate cancer therapeutics. Current Opinion in Oncology. https://doi.org/10.1097/CCO.0000000000000276.

[9] Averna, T.A., Kline, E.E., Smith, A.Y., Sillerud, L.O., Feb 2005. A decrease in 1H nuclear magnetic resonance spectroscopically determined citrate in human seminal fluid accompanies the development of prostate adenocarcinoma. The Journal of Urology 173(2):433–438. https://doi.org/10.1097/01.ju.0000148949.72314.d7.

[10] Barron, E.S., Huggins, C., Jun 1946. The citric acid and aconitase content of the prostate. Proceedings of the Society for Experimental Biology and Medicine 62(2):195 [Online]. Available: http://www.ncbi.nlm.nih.gov/pubmed/20993166.

[11] Costello, L.C., Franklin, R.B., Dec 01 2016. A comprehensive review of the role of zinc in normal prostate function and metabolism; and its implications in prostate cancer. Archives of Biochemistry and Biophysics 611:100–112. https://doi.org/10.1016/j.abb.2016.04.014.

[12] Costello, L.C., Franklin, R.B., 2006. The clinical relevance of the metabolism of prostate cancer; zinc and tumor suppression: connecting the dots. Molecular Cancer 5:17. https://doi.org/10.1186/1476-4598-5-17.

[13] Wu, X., Daniels, G., Lee, P., Monaco, M.E., 2014. Lipid metabolism in prostate cancer. American Journal of Clinical and Experimental Urology 2(2):111–120 [Online]. Available: https://www.ncbi.nlm.nih.gov/pubmed/25374912.

[14] Bezzi, M., Seitzer, N., Ishikawa, T., Reschke, M., Chen, M., Wang, G., et al., Jan 8 2018. Diverse genetic-driven immune landscapes dictate tumor progression through distinct mechanisms. Nature Medicine. https://doi.org/10.1038/nm.4463.

[15] Chen, J., Guccini, I., Di Mitri, D., Brina, D., Revandkar, A., Sarti, M., et al., Jan 15 2018. Compartmentalized activities of the pyruvate dehydrogenase complex sustain lipogenesis in prostate cancer. Nature Genetics. https://doi.org/10.1038/s41588-017-0026-3.

[16] Kobus, T., Wright, A.J., Weiland, E., Heerschap, A., Scheenen, T.W., Jan 2015. Metabolite ratios in 1H MR spectroscopic imaging of the prostate. Magnetic Resonance in Medicine 73(1):1–12. https://doi.org/10.1002/mrm.25122.

[17] Thomas, M.A., Nagarajan, R., Huda, A., Margolis, D., Sarma, M.K., Sheng, K., et al., Jan 2014. Multidimensional MR spectroscopic imaging of prostate cancer in vivo. NMR in Biomedicine 27(1):53–66. https://doi.org/10.1002/nbm.2991.

[18] Gholizadeh, N., Greer, P.B., Simpson, J., Goodwin, J., Fu, C., Lau, P., et al., Jul 19 2021. Diagnosis of transition zone prostate cancer by multiparametric MRI: added value of MR spectroscopic imaging with sLASER volume selection. Journal of Biomedical Science 28(1):54. https://doi.org/10.1186/s12929-021-00750-6.

[19] Braadland, P.R., Giskeødegård, G., Sandsmark, E., Bertilsson, H., Euceda, L.R., Hansen, A.F., et al., Mar 20 2018. Ex vivo metabolic fingerprinting identifies biomarkers predictive of prostate cancer recurrence following radical prostatectomy. British Journal of Cancer 118(6):e11. https://doi.org/10.1038/bjc.2017.470.

[20] Zheng, H., Zhu, Y., Shao, X., Cai, A., Dong, B., Xue, W., et al., Sep 4 2020. Distinct metabolic signatures of hormone-sensitive and castration-resistant prostate cancer revealed by a (1)H NMR-based metabolomics of biopsy tissue. Journal of Proteome Research 19(9):3741–3749. https://doi.org/10.1021/acs.jproteome.0c00282.

[21] Gonthier, K., Poluri, R.T.K., Audet-Walsh, E., Jul 2019. Functional genomic studies reveal the androgen receptor as a master regulator of cellular energy metabolism in prostate cancer. The Journal of Steroid Biochemistry and Molecular Biology 191:105367. https://doi.org/10.1016/j.jsbmb.2019.04.016.

[22] Chen, C.L., Lin, C.Y., Kung, H.-S., 2021. Targeting nitochondrial OXPHOS and their regulatory signals in prostate cancers. International Journal of Molecular Sciences 22(13435):24.

[23] Harkonen, P., Isotalo, A., Santti, R., Oct 1975. Studies on the mechanism of testosterone action on glucose metabolism in the rat ventral prostate. Journal of Steroid Biochemistry 6(10):1405–1413 [Online]. Available: https://www.ncbi.nlm.nih.gov/pubmed/1052841.

[24] Harkonen, P.L., Kostian, M.L., Santti, R.S., Mar 1982. Indirect androgenic control of citrate accumulation in rat ventral prostate. Archives of Andrology 8(2):107–116 [Online]. Available: https://www.ncbi.nlm.nih.gov/pubmed/6803691.

[25] Schopf, B., Weissensteiner, H., Schäfer, G., Fazzini, F., Charoentong, P., Naschberger, A., et al., Mar 20 2020. OXPHOS remodeling in high-grade prostate cancer involves mtDNA mutations and increased succinate oxidation. Nature Communications 11(1):1487. https://doi.org/10.1038/s41467-020-15237-5.

[26] Schopf, B., Schäfer, G., Weber, A., Talasz, H., Eder, I.E., Klocker, H., et al., Jun 2016. Oxidative phosphorylation and mitochondrial function differ between human prostate tissue and cultured cells. FEBS Journal 283(11):2181–2196. https://doi.org/10.1111/febs.13733.

[27] Bednarova, S., Lindenberg, M.L., Vinsensia, M., Zuiani, C., Choyke, P.L., Turkbey, B., Jun 2017. Positron emission tomography (PET) in primary prostate cancer staging and risk assessment. Translational Andrology and Urology 6(3):413–423. https://doi.org/10.21037/tau.2017.03.53.

[28] Giovacchini, G., Giovannini, E., Leoncini, R., Riondato, M., Ciarmiello, A., Sep 2017. PET and PET/CT with radiolabeled choline in prostate cancer: a critical reappraisal of 20 years of clinical studies. European Journal of Nuclear Medicine and Molecular Imaging 44(10):1751–1776. https://doi.org/10.1007/s00259-017-3700-x.

[29] Beauregard, J.M., Blouin, A.C., Fradet, V., Caron, A., Fradet, Y., Lemay, C., et al., Mar 03 2015. FDG-PET/CT for pre-operative staging and prognostic stratification of patients with high-grade prostate cancer at biopsy. Cancer Imaging 15:2. https://doi.org/10.1186/s40644-015-0038-0.

[30] Harkonen, P., Oct 1981. Androgenic control of glycolysis, the pentose cycle and pyruvate dehydrogenase in the rat ventral prostate. Journal of Steroid Biochemistry 14(10):1075–1084 [Online]. Available: https://www.ncbi.nlm.nih.gov/pubmed/7300327.

[31] Liu, Y., Franklin, R.B., Costello, L.C., Jan 01 1997. Prolactin and testosterone regulation of mitochondrial zinc in prostate epithelial cells. The Prostate 30(1): 26–32 [Online]. Available: https://www.ncbi.nlm.nih.gov/pubmed/9018332.

[32] Costello, L.C., Liu, Y., Franklin, R.B., Jul 1995. Testosterone stimulates the biosynthesis of m-aconitase and citrate oxidation in prostate epithelial cells. Molecular and Cellular Endocrinology 112(1):45–51. https://doi.org/10.1016/0303-7207(95)03582-r.

[33] Costello, L.C., Franklin, R.B., 1989. Prostate epithelial cells utilize glucose and aspartate as the carbon sources for net citrate production. The Prostate 15(4): 335–342 [Online]. Available: https://www.ncbi.nlm.nih.gov/pubmed/2594584.

[34] Lacouture, A., Jobin, C., Weidmann, C., Berthiaume, L., Bastien, D., Laverdière, I., et al., 2021. A FACS-free purification method to study estrogen signaling, organoid formation, and metabolic reprogramming in mammary epithelial cells. Frontiers in Endocrinology 12(672466).

[35] Fiehn, O., 2016. Metabolomics by gas chromatography–mass spectrometry: combined targeted and untargeted profiling. Current Protocols in Molecular Biology 114(1), 2021/06/17/15:38:26 [Online]. Available: https://onlinelibrary.wiley.com/doi/10.1002/0471142727.mb3004s114.

[36] Patel, D.P., Krausz, K.W., Xie, C., Beyoğlu, D., Gonzalez, F.J., Idle, J.R., 2017. Metabolic profiling by gas chromatography-mass spectrometry of energy metabolism in high-fat diet-fed obese mice. PLoS One 12(5):e0177953, 2021/06/17/15:40:49 [Online]. Available: https://dx.plos.org/10.1371/journal.pone.0177953.

[37] Deblois, G., Smith, H.W., Tam, I.S., Gravel, S.P., Caron, M., Savage, P., et al., Jul 12 2016. ERRalpha mediates metabolic adaptations driving lapatinib resistance in breast cancer. Nature Communications 7:12156. https://doi.org/10.1038/ncomms12156.

[38] McGuirk, S., Gravel, S.P., Deblois, G., Papadopoli, D.J., Faubert, B., Wegner, A., et al., Dec 05 2013. PGC-1 alpha supports glutamine metabolism in breast cancer. Cancer & Metabolism 1(1):22. https://doi.org/10.1186/2049-3002-1-22.

[39] McCray, T., Pacheco, J.V., Loitz, C.C., Garcia, J., Baumann, B., Schlicht, M.J., et al., Jan 22 2021. Vitamin D sufficiency enhances differentiation of patient-derived prostate epithelial organoids. iScience 24(1):101974. https://doi.org/10.1016/j.isci.2020.101974.

[40] Richards, Z., McCray, T., Marsili, J., Zenner, M.L., Manlucu, J.T., Garcia, J., et al., Feb 22 2019. Prostate stroma increases the viability and maintains the branching phenotype of human prostate organoids. iScience 12:304–317. https://doi.org/10.1016/j.isci.2019.01.028.

[41] Drost, J., Karthaus, W.R., Gao, D., Driehuis, E., Sawyers, C.L., Chen, Y., et al., Feb 2016. Organoid culture systems for prostate epithelial and cancer tissue. Nature Protocols 11(2):347–358. https://doi.org/10.1038/nprot.2016.006.

[42] Karthaus, W.R., Iaquinta, P.J., Drost, J., Gracanin, A., van Boxtel, R., Wongvipat, J., et al., Sep 25 2014. Identification of multipotent luminal progenitor cells in human prostate organoid cultures. Cell 159(1):163–175. https://doi.org/10.1016/j.cell.2014.08.017.